



Research paper

Phase junction CdS: High efficient and stable photocatalyst for hydrogen generation



Zizheng Ai, Gang Zhao, Yueyao Zhong, Yongliang Shao, Baibiao Huang, Yongzhong Wu*, Xiaopeng Hao*

State Key Lab of Crystal Materials, Shandong University, Jinan 250100, PR China

ARTICLE INFO

Keywords:

CdS
Photocorrosion
Phase junction
Photocatalytic activity

ABSTRACT

CdS is a photocatalyst known for its desirable bandgap and availability but it is limited by photocorrosion and inefficiency issues in practical applications. According to band engineering theory, regulating the width of bonding region that exists between cubic phase and hexagonal phase, we design a suitable phase junction and achieve effective separation of electron-hole pairs. Thus, the problems caused by photocorrosion and phase exclusion can be resolved. The optimal photocatalytic activity of the prepared material is $4.9 \text{ mmol h}^{-1} \text{ g}^{-1}$ with 41.5% quantum efficiency at the wavelength of 420 nm, which is 60 times higher than that of the initial samples (cubic or hexagonal phase), and keeps high photocatalytic stability. This novel construction approach can be useful in designing ideal band structures and matching the phase bandgap of other binary sulfides.

1. Introduction

New and sustainable technologies for H_2 production are needed due to the shortage of traditional energy resources worldwide. Hydrogen can be used as a replacement to fossil fuel because it is environmentally friendly, reproducible and sustainable. Solar-driven water-splitting reaction is one of the best approaches to obtain hydrogen. In order to gain full and efficient utilisation of solar energy, much attention has been paid to semiconductor photocatalysts at home and abroad. Particularly, transition metal chalcogenides [1] are ideal candidates for semiconductor-based photocatalytic technology. CdS may be used as potential material for photocatalytic water splitting due to its suitable bandgap ($E_g = 2.42 \text{ eV}$) and relatively negative conduction band [2–4], which can efficiently absorb visible light and reduce water to produce H_2 . However, its application is limited by the rapid charge carrier recombination and poor stability under visible light [5,6].

Various strategies have been employed to resolve its drawbacks to inhibit the charge carrier recombination effectively and improve the stability of CdS. On the one hand, the integration of CdS with other materials has been adopted in many reports, which forms the hetero-nanostructured photocatalysts or surface modification of CdS, such as CdS/rGO [7], MoS_2/CdS [8,9] and N-doped graphene/CdS [10]. Whilst the photocatalytic H_2 production activity of CdS is improved, the stability can be further enhanced. Further simplifying these methods is also possible. On the other hand, the high photocatalytic H_2 can be

indeed achieved with the assistance of Rh, Au, Ru, and Pt noble metals, but a broader range of applications is limited because of their scarcity and costs [11,12]. Hence, new tactics to ameliorate photocatalytic performance of CdS-based photocatalysts need to be developed.

Intensive researches have focused on the morphology [13], crystallinity and particle size [14,15] of CdS. For example, using solvothermal synthesis, Chen et al. [16] and Gao et al. [17] reported multi-armed CdS nanorods in ethylenediamine, whereas Wang et al. [18] synthesised CdS multipods in dodecylamine. In terms of the methods above, the performance of CdS can be improved to some extent, and investigating the crystal structure of CdS is necessary for further improvement. Phase junction in some semiconductor compounds with multiple crystal phases has been proven to reliably lead to enhanced photocatalytic performance. One of the cross-sectional examples is P25 (Degussa TiO_2), a common photocatalyst that is made up of anatase and rutile TiO_2 . As a matter of fact, P25 exhibits better photocatalytic activity than either rutile or anatase TiO_2 [19]. Researchers also have found similar phenomena in Ga_2O_3 [20] and CaTa_2O_6 [21] nanoparticles with phase junction. Nevertheless, application of CdS encounters difficulties upon the formation of the phase junction. Bao and Shen et al. found that hexagonal-cubic CdS nanocrystals showed worse photocatalytic activity than hexagonal or cubic phase CdS nanocrystals alone. This phenomenon was attributed to the crystalline defects occurring at the interface of the two phases [22]. By inserting Pt into the phase junction of core-shell hexagonal-cubic CdS nanoparticles,

* Corresponding author.

E-mail address: xphao@sdu.edu.cn (X. Hao).

<http://dx.doi.org/10.1016/j.apcatb.2017.09.002>

Received 26 June 2017; Received in revised form 10 August 2017; Accepted 2 September 2017

Available online 06 September 2017

0926-3373/ © 2017 Elsevier B.V. All rights reserved.

Hoffmann and co-workers successfully eliminated the surface states of hexagonal CdS core and improved photocatalytic H_2 production rate [23]. Through synthesising hexagonal-cubic core-shell nanorods, Li and Han improved the CdS photocatalytic activity [24]. Although the phase junction has been studied to some extent via above methods, the importance of phase junction has not been taken much concern really. Therefore, further studies on the phase junction are still needed.

Band engineering is important to acquire suitable band structures and facilitates the separation of electron-hole pairs. Using this concept, we designed an appropriate phase junction by regulating the bonding region width between cubic phase and hexagonal phase for the first time. The bonding region widths were studied to realise band structures with high H_2 conversion rate ($4.9 \text{ mmol h}^{-1} \text{ g}^{-1}$ with 41.5% quantum efficiency). In addition, phase junctions with suitable bonding region widths have long-term stability of photocatalytic activity. This present strategy could be used as a basis to design binary sulfides and other related materials.

2. Experimental section

2.1. Materials

Cadmium nitrate ($\text{Cd}(\text{NO}_3)_2 \cdot 4\text{H}_2\text{O}$) and sodium sulfide ($\text{Na}_2\text{S} \cdot 9\text{H}_2\text{O}$) were purchased from Aladdin. Ammonia solution ($\text{NH}_3 \cdot \text{H}_2\text{O}$), absolute ethanol and lactic acid provided by Sinopharm Chemical Reagent Co. Ltd. (Shanghai) were of analytical reagent grade. All materials were used as received without further purification. Solutions were prepared freshly with deionised water.

2.2. Synthesis of preliminary CdS nanoparticles

CdS nanoparticles were prepared by a one-step hydrothermal method. Keeping the molar proportion of Cd/S equal to 1:1, 0.925 g Cd ($\text{NO}_3)_2 \cdot 4\text{H}_2\text{O}$ and 0.721 g $\text{Na}_2\text{S} \cdot 9\text{H}_2\text{O}$ were dissolved in 20 mL ammonium chloride (ammonia) solution, with concentration of 1%, 3%, 5%, 7% and 9%. Subsequently, the solutions were agitated using a magnetic stirrer for 15 min and placed in a 25 mL Teflon-lined autoclave and maintained for 24 h at temperatures of 150 °C, 180 °C, 200 °C and 220 °C. The products with optimal concentration of 5% ammonia solution were used for hydrothermal treatment at reaction times of 3, 6, 9, 12, 15, 18, 21 and 27 h to further study the influence of the bonding region width. After cooling to room temperature, the precipitate was filtered, washed with ethanol and water several times and dried at 80 °C for 24 h in a vacuum drying chamber.

2.3. Characterisations

Powder X-ray diffraction (XRD) patterns were recorded on a Bruker D8-Advance X-ray powder diffractometer with a $\text{Cu-K}\alpha$ radiation ($\lambda = 0.15418 \text{ nm}$). Scanning electron microscopy (SEM) images were collected using a Hitachi S-4800 microscope equipped with an energy-

dispersive X-ray analyser (EDS, Horiba EMAX Energy EX-350). TEM and HRTEM images were obtained with a Philips Tecnai 20U-Twin microscope at an acceleration voltage of 200 kV. UV-vis diffuse reflectance spectroscopy (DRS) was conducted using a Shimadzu UV2550 recording spectrophotometer equipped with an integrating sphere with wavelength of 200 nm to 900 nm. BaSO_4 was used as a reference. The room-temperature Raman spectra of samples were recorded on a LabRam HR system from Horiba Jobin Yvon at room temperature using the 532 nm solid laser as the exciting source. X-ray photoelectron spectroscopy (XPS, Thermo ESCALAB 250) was performed using monochromated Al-K α radiation (1486.8 eV). The fluorescent lifetime was obtained by Opolette 355 II Instrument (USA).

2.4. Photocatalytic activity test

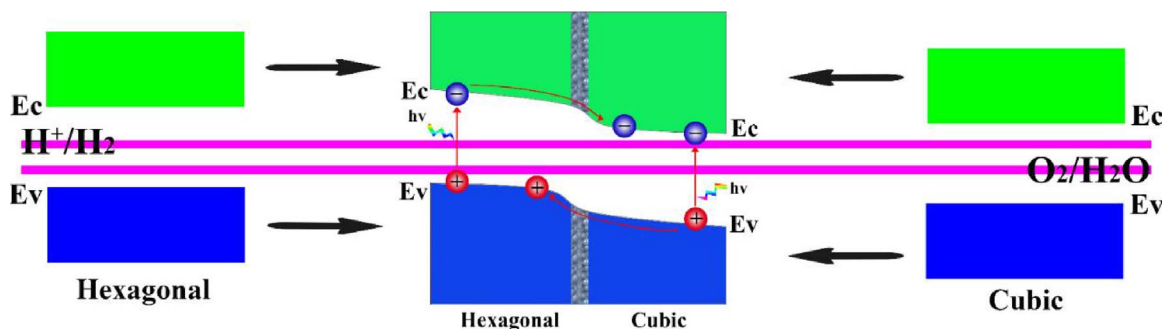
Photocatalytic reactions were carried out in a Pyrex reaction cell connected to a closed gas circulation and evacuation system. Fifty milligrams of catalysts were dispersed in 100 mL of aqueous solution containing 20 mL of lactic acid as sacrificial agents. The suspension was then thoroughly degassed and irradiated by a Xe lamp (300 W) equipped with an optical cutoff filter ($\lambda = 420 \text{ nm}$) to eliminate ultraviolet light. The temperature of the reactant solution was maintained at 5 °C during the reaction. The amount of H_2 produced from water-splitting was analysed using online gas chromatography (Gc7900 Tianmei Shanghai China). The photocatalytic activity of the CdS nanoparticles was assessed by the average rate of H_2 evolution in 5 h.

2.5. Photoelectrochemical activity measurements

The PEC measurement system in this study was a CHI660D workstation (Shanghai Chenhua, China) with a three-electrode configuration using the as-obtained samples as the working electrodes, a Pt plate as the counter electrode, Ag/AgCl as the reference electrode and a 300 W Xe lamp equipped with an optical cutoff filter ($\lambda = 420 \text{ nm}$) as the light source. Na_2SO_4 aqueous solution (0.5 M) with 20% lactic acid was used as the electrolyte. The working electrodes were prepared as follows: 10 mg of as-prepared nanoparticles were dispersed in absolute ethanol and the suspension was directly deposited onto an FTO conductive glass plate and then dried at 80 °C in a vacuum oven.

3. Band engineering design theory

CdS possesses two typical structures: hexagonal phase and cubic phase. Given the disparity of bandgaps between cubic phase and hexagonal phase, band bending exists when the two phases contact each other. Further integrating band engineering theory with phase junction, the concept of band structure with high hydrogen production is shown in Scheme 1. In these two phases, the electron-hole pairs recombine quickly due to the limitation of their own band structure. As the hexagonal phase possesses higher conduction band level than the cubic phase, the photo-generated electrons transfer from the conduction band



Scheme 1. Schematic theories illustrating the regulation of band structure through phase junction with bonding region.

of hexagonal phase to the conduction band of cubic phase. Meanwhile the corresponding photo-generated holes transfer from the valence band of cubic phase to the valence band of hexagonal phase. With the formation of bonding region, the phase junction can be further optimised. Through regulating the bonding region width, the photo-generated electrons can effectively transfer to the conduction band of cubic phase. A suitable bonding region width can act as an energy transition area to minimise the energy loss from conduction level differences between cubic phase and hexagonal phase and as a shelter to prevent the recombination of electron-hole pairs. Based on the above analysis, to design and build suitable band structure through the phase junction, an appropriate bonding region is essential.

4. Results and discussion

4.1. Morphology and structure characterisation of the CdS nanoparticles

4.1.1. Morphology and size changes

Sphere-like CdS nanoparticles were synthesised through a one-step hydrothermal method at 200 °C with different concentrations of ammonia solution and hydrothermal time. The morphology of CdS nanoparticles is illustrated in Fig. 1a. The shape of particles gradually turned from amorphous to sphere-like structures with increasing concentrations of ammonia solution (Fig. S1). For different hydrothermal time, the particle size gradually decreased to 33.48 nm from the initial 44.8 nm and gradually increased to 42.4 nm with prolonged reaction time (Fig. S2). The optimal size was 33.48 nm when hydrothermal time was 18 h. As a contributing factor, an appropriate particle size with higher specific surface area may be better (Fig. S3) because the high absorption area can fully utilise the incident light and enhance the

speed of electronic delivery [25].

In addition, the UV–vis diffuse absorption spectra results of CdS nanoparticles with optimal performance at different hydrothermal temperatures are shown in Fig. 1b. The CdS nanoparticles with cubic phase or hexagonal phase have lower intensity of absorbance than CdS nanoparticles with the phase junction. This phase junction could modify the bandgap contact between the cubic phase and hexagonal phase and finally make the general bandgap width suitable for visible light range [26]. The width of the bandgap can further confirm the importance of phase junction (Fig. S4). CdS nanoparticles with phase junction have a bandgap of $E_g = 1.97$ eV, those with cubic phase $E_g = 2.19$ eV and those with hexagonal phase $E_g = 2.09$ eV. Therefore, absorption spectrometry can be expanded to visible light with wavelengths more than 600 nm, which significantly improves the utilisation of the incident light source.

4.1.2. Identification of structure

The XRD patterns of CdS are shown in Fig. 1c. CdS shows neat cubic phase (at 1%) at first, and then hexagonal phase is established gradually along with the increase in concentration of ammonia solution. The optimal proportional degree of mixing results in the best performance. Subsequently, the hexagonal phase becomes predominant and gradually transforms into pure hexagonal phase (at 9%). The thermodynamics and kinetics analyses are shown in Fig. S5. In addition, the crystallinity of CdS particles are also found in different hydrothermal times (Fig. S6). Therefore, a phase junction of *meta*-stable cubic phase and stable hexagonal phase can exist in CdS nanoparticles. The phase was originally cubic, which is supported by the emergence of the (111), (220) and (311) diffraction peaks of cubic CdS phase (Fig. 1c). However, as the (200) plane is perpendicular to the (002) plane, the

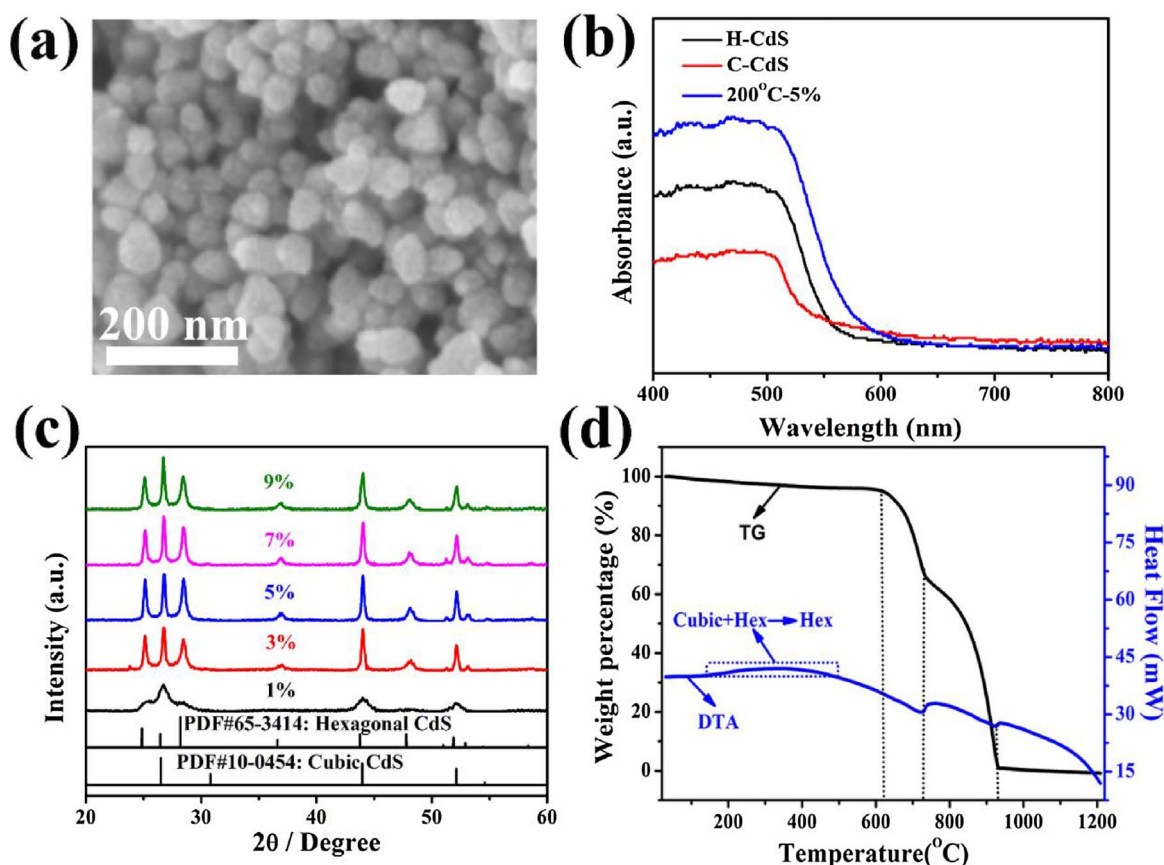


Fig. 1. Initiatory CdS nanoparticles (prepared at 200 °C for 18 h). (a) SEM image of CdS nanoparticles synthesised with an ammonia concentration of 5%. (b) UV–vis DRS on CdS nanoparticles with different phase structures (hexagonal phase, cubic phase, 200 °C-5%). (c) XRD patterns of CdS nanoparticles prepared with different concentration of ammonia solution. (d) TG-DTA curves of CdS nanoparticles prepared with an ammonia concentration of 5%.

intensity of a peak corresponding to this plane will be much reduced, and may not be observable [27]. This may be the reason for the absence of the (200) peak of cubic CdS phase. Afterwards, the (100) and (101) characteristic diffraction peaks of hexagonal CdS show up, and their intensities are increasing. Meanwhile, the intensity of the (102) is increasing. Thus, the phase transition occurs until the cubic phase is replaced completely.

To make the co-existence of cubic and hexagonal CdS more convincing, TG-DTA was performed (Fig. 1d). TG-DTA curves of CdS nanoparticles include a four-step process. An initial weight loss ($\sim 2.2\%$) step occurs at around 180°C , which can be attributed to the evaporation of absorbed water and ethanol. Subsequently, a tardy exothermic peak exists between 200°C and 480°C from the DTA curve maintaining the constant weight of the samples, which demonstrates the phase transition from hexagonal and cubic phases to a single stable hexagonal phase, which could be further demonstrated by the XRD pattern contrast change of CdS nanoparticles before and after calcination (Fig. S7). The transformation coincides with TG-DTA curves between 200°C and 480°C . Therefore, the phase co-existence is identified indirectly. Afterwards, the decomposition of sample starts at 630°C and decomposes totally at 930°C .

In addition, Raman spectroscopy analysis (Fig. S8) shows the co-existence of cubic phase and hexagonal phase of CdS [28,29]. The TEM image of CdS (prepared with a concentration of 5% at 200°C for 18 h) shows sphere-like morphology (Fig. 2a). Fig. 2b shows the HRTEM image of CdS nanoparticles. There are two representative crystal planes belonging to hexagonal phase and cubic phase and a bonding region between them. As stated above, the phase junction can be created

effectively using the ammonia-aided hydrothermal method. XPS was used to study the composition and electronic structure of the as-obtained CdS nanoparticles. As shown in Fig. S9, full XPS spectra consist of Cd, S and C elements. Among them, C can be excluded from the product as base materials. The Cd 3d high-resolution XPS (Fig. 2c) displays two peaks at 405 and 411.75 eV, which are consistent with the peaks of Cd 3d in pure CdS nanoparticles. The high-resolution XPS (Fig. 2d) of S 2p have two peaks at 161.25 and 162.4 eV, which correspond to the pure CdS nanoparticles [30]. The atom ratio of the CdS nanoparticles is S/Cd = 1.521, which indicated that the extra S^{2-} forms the S vacancy defects as scavenger for the photo-generated holes to separate the photo-generated electron-hole pairs [31].

4.2. The properties of photocatalytic H_2 evolution

The photocatalytic H_2 production performance of CdS with different concentration of ammonia solution at 200°C is measured (Fig. 3a). The CdS nanoparticles with cubic structure at 1% exhibit poor H_2 evolution ability ($0.0824 \text{ mmol h}^{-1} \text{ g}^{-1}$) because of the wide bandgap [32]. Subsequently, with the increase of ammonia concentration, the cubic phase gradually changed into hexagonal phase in CdS nanoparticles and finally transformed to a total hexagonal phase at a concentration of 9% (Fig. 1c). The rate of hydrogen-producing CdS nanoparticles improves rapidly. However, when the concentration of ammonia is 5%, the H_2 evolution rate is more effective than other concentrations of ammonia and the highest H_2 conversion rate is $4.9 \text{ mmol h}^{-1} \text{ g}^{-1}$ (Fig. 3b), which is 60 times higher than the initial sample. This rate corresponds to an apparent quantum efficiency of 41.5% ($\lambda_{\text{ex}} = 420 \text{ nm}$) (S10). In

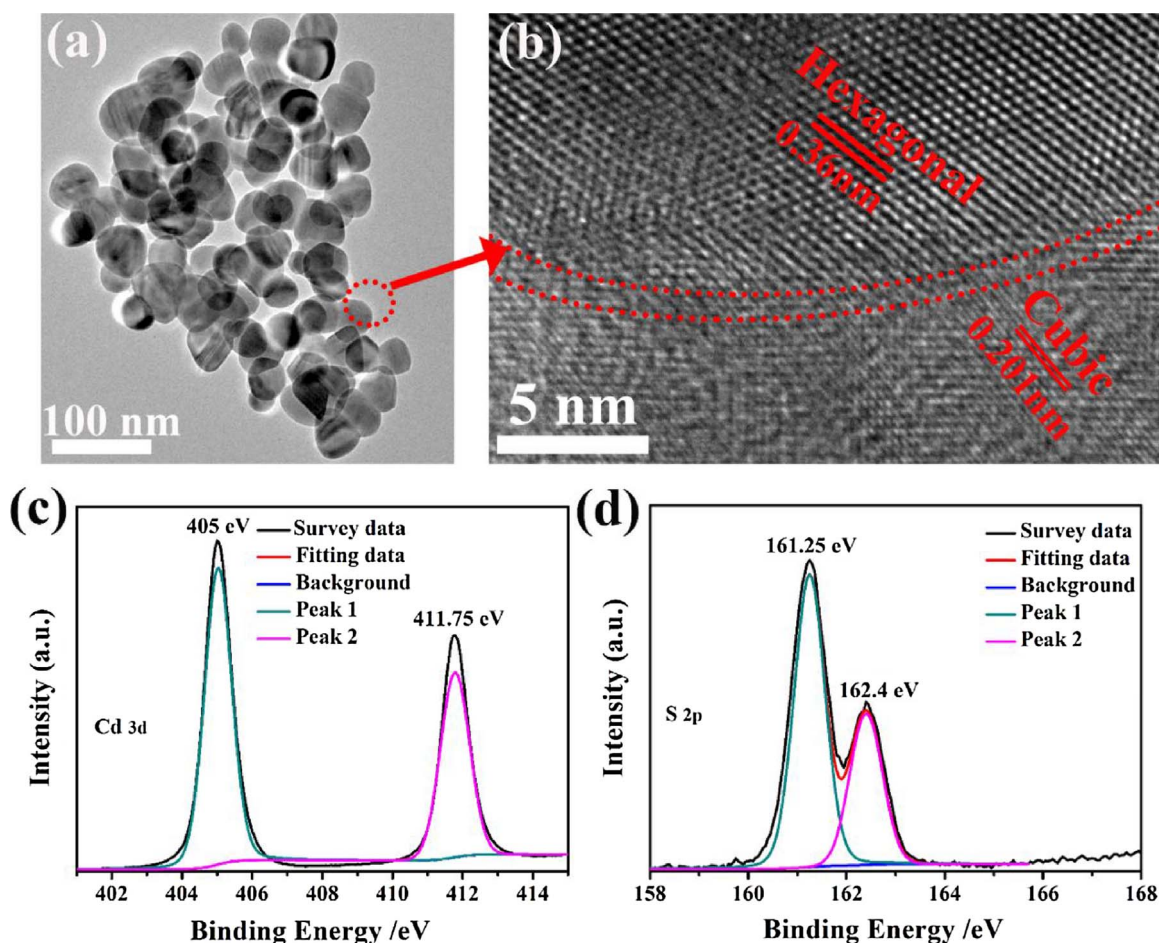


Fig. 2. Initiatory CdS nanoparticles (prepared with a concentration of 5% at 200°C for 18 h). (a) TEM image of CdS nanoparticles. (b) HRTEM image of CdS nanoparticles with different phase structure. XPS spectra of CdS nanoparticles: (c) Cd 3d states, (d) S 2p states.

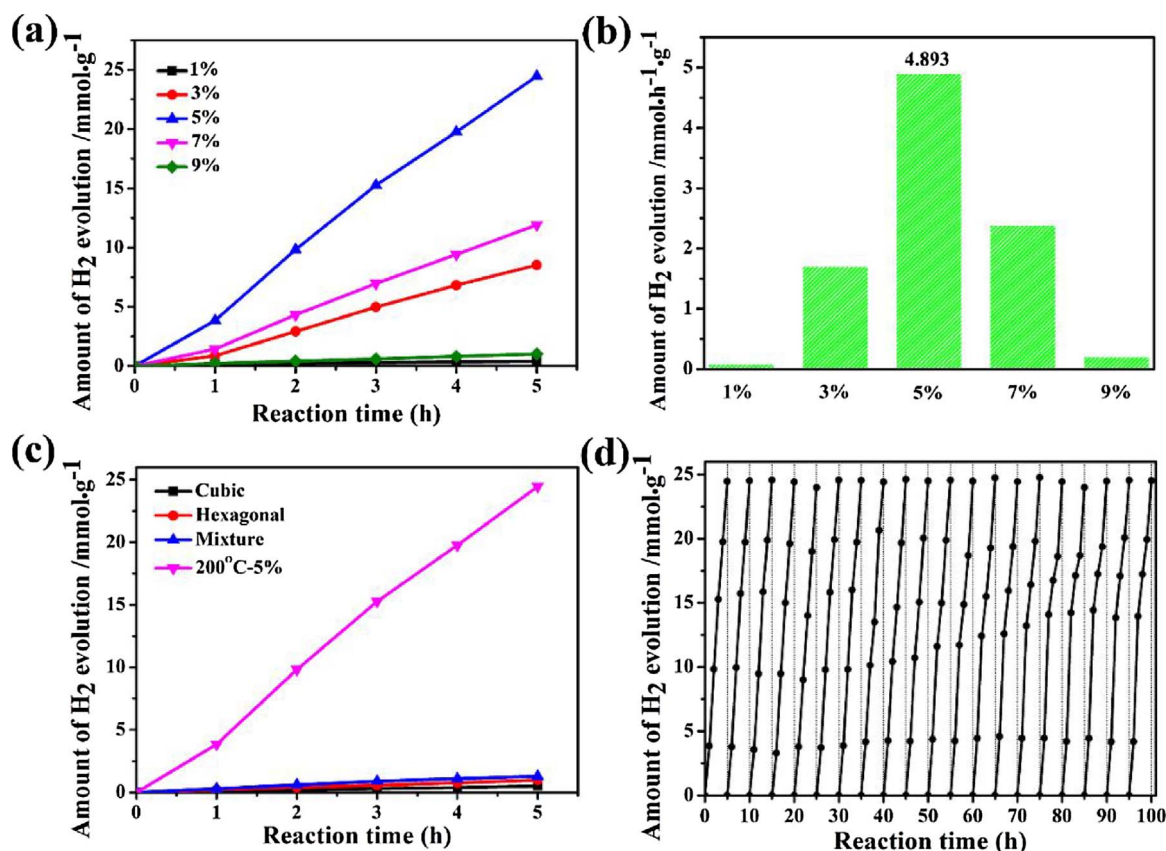


Fig. 3. Photocatalytic performances of CdS nanoparticles (prepared at 200 °C for 18 h). (a) The photocatalytic H₂ production activity of CdS nanoparticles prepared with different ammonia concentration. (b) H₂ evolution rates of CdS nanoparticles prepared with different ammonia concentration. (c) The photocatalytic H₂ production activity of CdS nanoparticles with different phase structures (hexagonal phase, cubic phase, miscible phase, 200 °C-5%). (d) The photocatalytic H₂ evolution stability of CdS nanoparticles (prepared with an ammonia concentration of 5% at 200 °C for 18 h). Conditions: 0.05 g catalyst, 100 mL aqueous solution with 20 mL lactic acid and 300 W Xe lamp with an optical cutoff filter ($\lambda > 420$ nm).

other hydrothermal temperatures, the photocatalytic H₂ production activity with different concentrations of ammonia was also investigated as shown in Fig. S11, in which the best photocatalytic H₂ production performance can be obtained with different concentrations of ammonia. This phenomenon explains indirectly that there is a relationship between hydrothermal temperature and concentration of ammonia. From the contrast in HER activity rate, the H₂ conversion rate is the highest when hydrothermal temperature is 200 °C. This comparison can testify the vital role of the phase junction with suitable bonding region width in improving its photocatalytic activity. To verify whether it is a simple combination effect of cubic and hexagonal phases, a mixture of CdS nanoparticles separately possessing cubic phase and hexagonal phase was used to measure the performance of photocatalytic H₂ evolution (Fig. 3c). The result demonstrates that CdS nanoparticles obtained with an ammonia concentration of 5% show far better property than this mixture. Instead, the H₂ evolution rate is reduced with further increase in the concentration, which can be explained by the following: the gradual formation of the phase junction between the cubic phase and the hexagonal phase in CdS nanoparticles plays a positive role; however, excessive formation of hexagonal phase leads to the reduction of the phase junction, thereby posing a negative effect.

The most optimal CdS nanoparticles prepared with an ammonia concentration of 5% is also used to test the photocatalytic stability. The hydrogen-producing reaction was performed for 100 h (Fig. 3d). After every five cycles, the CdS sample is re-dispersed in a 20% lactic acid solution to guarantee sufficient amount of the sacrificial agent. The H₂ evolution level can reach a stable high level at the beginning, and this level can be maintained after 100 h. Moreover, as shown in Fig. S12, the longer stability test shows that the high H₂ evolution level continues in 150 h and then drops gradually to 80%. Overall, compared to the

drawback of photo-corrosion of CdS nanoparticles (less than 11 h) without phase junction (Fig. S13), the long lifetime of the sample accounts for the robust phase junction. This aspect will be discussed in detail in the following section.

4.3. Mechanism for the enhanced photocatalysis via phase junction of CdS

In comparison to CdS with cubic or hexagonal phase, the as-obtained CdS synthesised through ammonia regulation possesses higher catalytic effects and longer lifetime because of the proper band structure with suitable bonding region width existing between the cubic and hexagonal phases. To investigate the formation mechanism of the bonding region, the CdS was synthesised with an optimal concentration of 5% under different hydrothermal time (1, 9, 18 and 27 h) (Fig. 4). The figure shows the changing trends of bonding region between cubic phase and hexagonal phase. The bonding region width about 0.21 nm can be found at first. As time increases to 18 h, the bonding region width reaches to 0.76 nm. Further increasing the hydrothermal time leads to an increase of the bonding region width to almost 2.66 nm. Through the regulation of the bonding region width, the band structure can be adjusted to the optimal state and the problem of the negative effects caused by direct contact between cubic phase and hexagonal phase is solved. Meanwhile the stability of phase junction is enhanced greatly. These results confirm the significance of the bond region with proper width, which agrees with the comparison of photocatalytic H₂ production activity with different hydrothermal times (Fig. S14) [33]. With the same concentration and time, the preparation of CdS under various hydrothermal temperatures was carried out to study the crystallinity (Fig. S15). The degree of crystallinity gets better as the temperature rises, and the temperature at 200 °C was found to be the best,

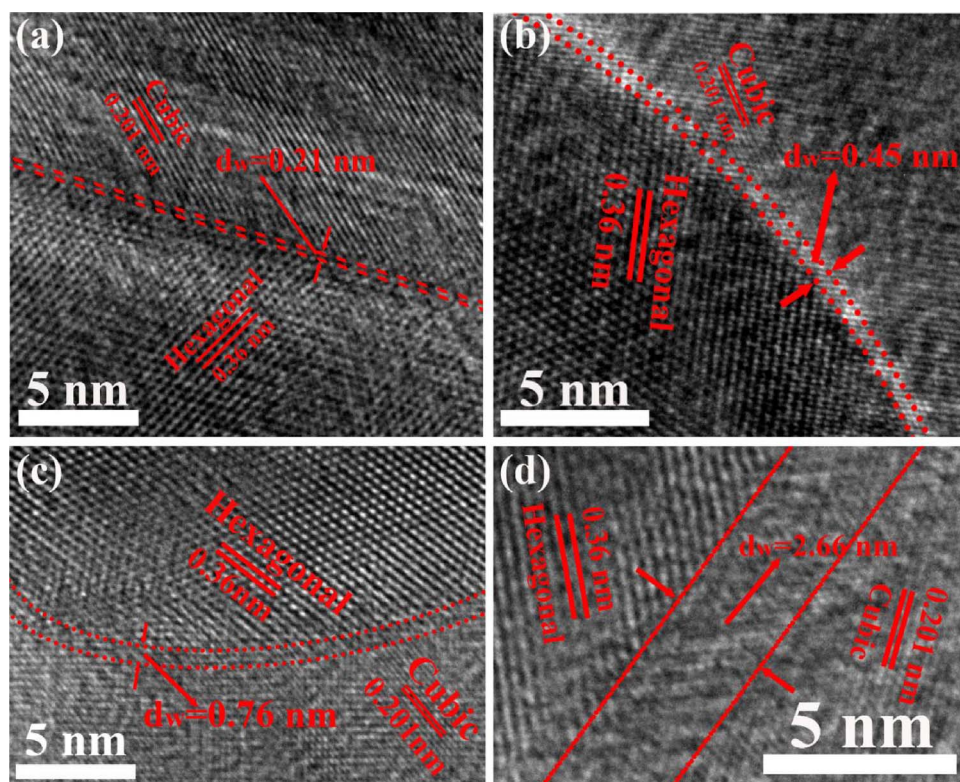


Fig. 4. The bonding region width of CdS nanoparticles prepared with different hydrothermal times (under the concentration of 5% at 200 °C). (a) 1 h, (b) 9 h, (c) 18 h and (d) 27 h.

because the most suitable crystallinity is formed [34].

The phase junction with suitable bonding region width between cubic and hexagonal phase plays a key role in boosting photocatalytic activity, which could be interpreted from the two aspects: the effective separation of photo-generated electrons and holes and the proper band structure modulation. As shown in Fig. 1c, the (101)/(111) ratio, representing the hexagonal and cubic phase respectively, increased with increasing concentration of ammonia and reached the highest level at 5% and then decreased gradually. This also can be confirmed by performance comparisons (Fig. 3a). Due to the disparity of band structure and electronic properties, the phase-junction-forming mechanism is similar to the type II semiconductor junctions (Fig. S16) [35], which can facilitate the separation of photo-generated electrons and holes, thereby accomplishing the goal of higher photocatalytic performance. When the suitable bonding region width is formed between cubic and hexagonal phase, it will act as the energy transition area to minimise the energy loss, which will also induce the internal electric field to segregate electrons and holes. The different levels of band structures drive the separated electrons to the cubic phase with the lower CB edge and holes to the hexagonal phase with the higher VB edge. When the band alignment of these two phases falls into the scope of a type II junction [36], the charge recombination can be suppressed due to the consistent charge migrations inside and outside the space charge region. Additionally, the suitable bonding region width can work as a shelter to prevent the recombination of electron-hole pairs. Therefore, the sacrificial reagent could scavenge the photo-generated holes fully and lower the recombination probability. Furthermore, the transient photocurrent experiment from samples with different bonding region widths confirmed the importance in reducing recombination probability of photo-generated electrons and holes and improving photocatalytic activity (Fig. 5a). CdS with cubic phase or hexagonal phase shows low photocurrent density due to the rapid recombination of photo-generated electrons and holes. After the formation of phase junction with suitable bonding region width, the photocurrent intensity shows significant increase, meaning that the photo-generated electron-hole pairs have a longer lifetime. It can be confirmed again from the

fluorescent lifetime spectra (Fig. S17), which exhibits that CdS nanoparticles with phase junction have longer lifetime than that of cubic and hexagonal phase. All above results indicate that the separation efficiency of electron-hole pairs can be improved greatly by forming suitable phase junction.

Another factor is the proper bandgap structures. The UV-vis absorption spectra show the bandgaps of CdS prepared with various concentrations of ammonia. According to the plot of the Kubelka-Munk function $[\alpha h\nu]^{1/2}$ versus the energy of absorbed light converted from the UV-vis absorption spectrum [37], the band gap of cubic phase and hexagonal phase is 2.19 eV and 2.09 eV respectively, with ammonia concentration of 1% and 9%. The most appropriate bandgap is 1.97 eV at the concentration of 5% (Fig. S4). The valence band (VB)-XPS provides the position of the VB. Subsequently, the CB position can be calculated according to the band gap. VB-XPS analysis (Fig. S18) shows that the VB maximum (VBM) position of hexagonal CdS is above the position of cubic CdS. Therefore, the CB of the hexagonal CdS is above the cubic CdS. In addition, the Mott-Schottky analyses of cubic phase, hexagonal phase and phase junction sample were conducted to study the electronic band structure of CdS nanoparticles (Fig. S19). It exhibits that they all belong to n-type semiconductor. The potential of the CB edge (E_{CB}) can be approximately estimated from the x-intercept in the MS plot. As for the cubic phase and hexagonal phase, the calculated E_{CB} is -1.69 V vs. SCE (-1.45 V vs. NHE) and -1.87 V vs. SCE (-1.63 V vs. NHE). The conduction band edge of phase junction is estimated to be -1.74 V vs. SCE (-1.5 V vs. NHE). The results also confirm that the CB of the hexagonal CdS is above that of the cubic CdS. Based on the UV-vis diffuse reflectance spectra, the schematic diagram of the CdS for hydrogen production under visible light irradiation is shown in Fig. 5b, which shows that the phase junction with suitable bonding region width is the key parameter that determines the efficiency of photocatalytic H_2 evolution.

To explore the cause of long photocatalytic lifetime, the stability of phase junction with suitable bonding region width was examined by HRTEM (Fig. 5c) and XRD (Fig. 5d) after 100 h reaction times. The results show that the phase junction still remains stable after prolonging

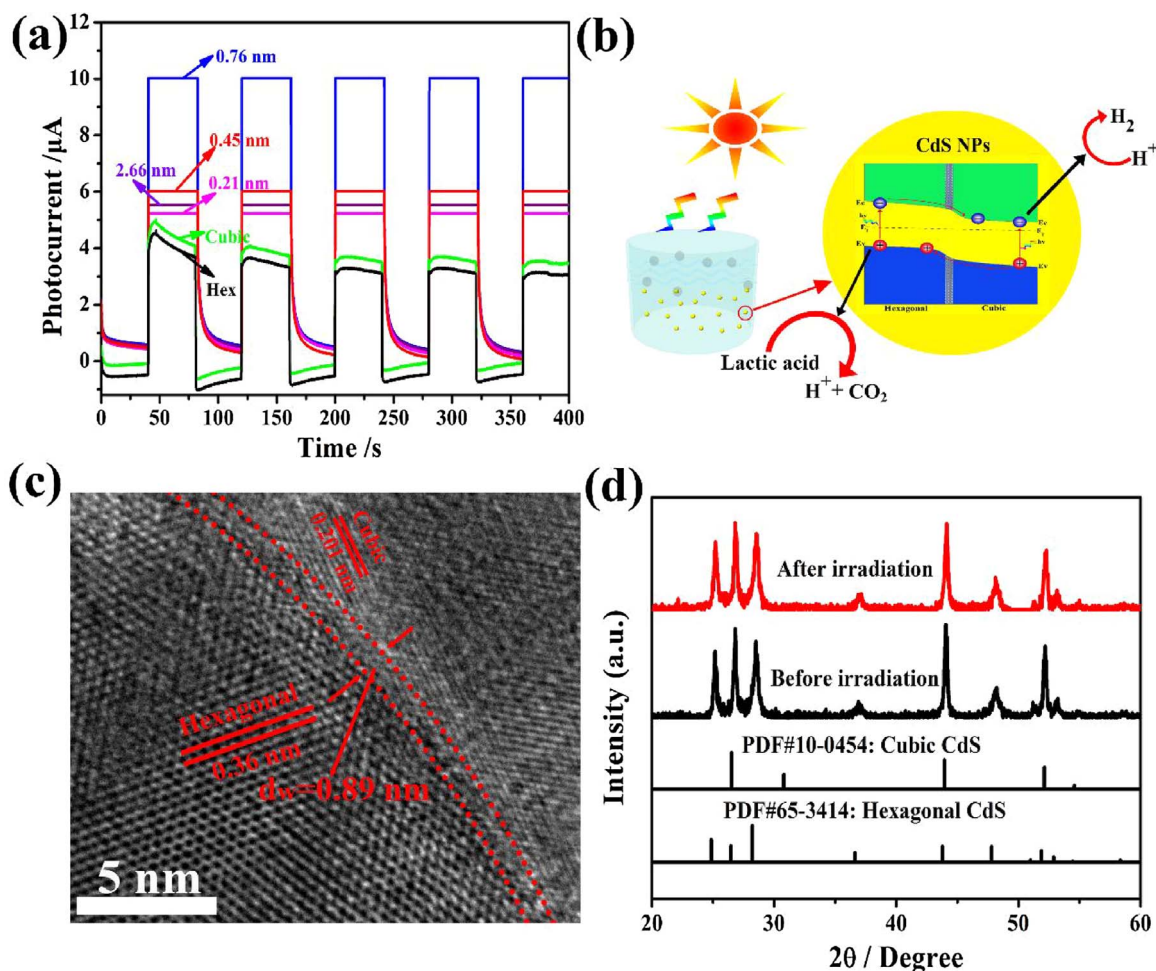


Fig. 5. The final CdS nanoparticles (prepared with an ammonia concentration of 5% at 200 °C for 18 h). (a) Transient photocurrent responses of CdS nanoparticles with different bonding region widths. (b) Schematic diagram of CdS nanoparticles for hydrogen production under visible light irradiation. (c) The HRTEM images of the CdS nanoparticles after irradiation for 100 h. (d) XRD patterns of CdS nanoparticles before and after the irradiation for 100 h.

reaction, showing that this construction is very stable and remains unchanged during the overall reaction. The main reason may be attributed to the suitable bonding region width, which can be the shield for phase junction.

5. Conclusion

We have designed and fabricated a novel CdS nano-photocatalyst with bonding-region-width-controlled phase junction. The phase junction can be optimised via the regulation of bonding region width between cubic phase and hexagonal phase. When the bonding region width is 0.76 nm, the phase junction can reach the best separation efficiency of electron-hole pairs and show the topmost photocatalytic activity ($4.9 \text{ mmol h}^{-1} \text{ g}^{-1}$ with 41.5% QE), which is 60 times higher than the initial sample (cubic or hexagonal phase). In the meantime, it has relatively high photocatalytic stability. This work might be useful in designing the proper band structure of other photocatalysts with phase junction for hydrogen revolution.

Acknowledgments

This work is supported by the National Natural Science Foundation of China (Contract No. 51572153, 51602177), the Fundamental Research Funds of Shandong University and Taishan Scholars Program of Shandong Province.

Appendix A. Supplementary data

Supplementary data associated with this article can be found, in the online version, at <http://dx.doi.org/10.1016/j.apcatb.2017.09.002>

References

- [1] Q.H. Wang, K. Kalantar-Zadeh, A. Kis, J.N. Coleman, M.S. Strano, *Nat. Nano* 7 (2012) 699–712.
- [2] J. Chen, X.J. Wu, L. Yin, B. Li, X. Hong, Z. Fan, B. Chen, C. Xue, H. Zhang, *Angew. Chem. Int. Ed.* 54 (2015) 1210–1214.
- [3] J.S. Jang, U.A. Joshi, J.S. Lee, *J. Phys. Chem. C* 111 (2007) 13280–13287.
- [4] D. Jing, L. Guo, *J. Phys. Chem. B* 110 (2006) 11139–11145.
- [5] Y.P. Xie, Z.B. Yu, G. Liu, X.L. Ma, H.-M. Cheng, *Energy Environ. Sci.* 7 (2014) 1895–1901.
- [6] H. Yan, J. Yang, G. Ma, G. Wu, X. Zong, Z. Lei, J. Shi, C. Li, *J. Catal.* 266 (2009) 165–168.
- [7] R. Lin, L. Shen, Z. Ren, W. Wu, Y. Tan, H. Fu, J. Zhang, L. Wu, *Chem. Commun.* 50 (2014) 8533–8535.
- [8] F. Ma, Y. Wu, Y. Shao, Y. Zhong, J. Lv, X. Hao, *Nano Energy* 27 (2016) 466–474.
- [9] Y. Liu, Y.-X. Yu, W.-D. Zhang, *J. Phys. Chem. C* 117 (2013) 12949–12957.
- [10] L. Jia, D.-H. Wang, Y.-X. Huang, A.-W. Xu, H.-Q. Yu, *J. Phys. Chem. C* 115 (2011) 11466–11473.
- [11] Z.B. Yu, Y.P. Xie, G. Liu, G.Q. Lu, X.L. Ma, H.-M. Cheng, *J. Mater. Chem. A* 1 (2013) 2773–2776.
- [12] F.E. Osterloh, *Chem. Mater.* 20 (2008) 35–54.
- [13] B.A. Simmons, S. Li, V.T. John, G.L. McPherson, A. Bose, W. Zhou, J. He, *Nano Lett.* 2 (2002) 263–268.
- [14] X. Peng, M.C. Schlamp, A.V. Kadavanich, A.P. Alivisatos, *J. Am. Chem. Soc.* 119 (1997) 7019–7029.
- [15] R. Banerjee, R. Jayakrishnan, R. Banerjee, P. Ayyub, *J. Phys. Condens. Matter* 12 (2000) 10647.
- [16] M. Chen, Y. Xie, J. Lu, Y. Xiong, S. Zhang, Y. Qian, X. Liu, *J. Mater. Chem.* 12 (2002)

- 748–753.
- [17] F. Gao, Q. Lu, S. Xie, D. Zhao, *Adv. Mater.* 14 (2002) 1537–1540.
- [18] X. Wang, Z. Feng, D. Fan, F. Fan, C. Li, *Cryst. Growth Des.* 10 (2010) 5312–5318.
- [19] K.L. Schulte, P.A. DeSario, K.A. Gray, *Appl. Catal. B: Environ.* 97 (2010) 354–360.
- [20] X. Wang, Q. Xu, M. Li, S. Shen, X. Wang, Y. Wang, Z. Feng, J. Shi, H. Han, C. Li, *Angew. Chem. Int. Ed.* 51 (2012) 13089–13092.
- [21] P. Wang, P. Chen, A. Kostka, R. Marschall, M. Wark, *Chem. Mater.* 25 (2013) 4739–4745.
- [22] N. Bao, L. Shen, T. Takata, K. Domen, A. Gupta, K. Yanagisawa, C.A. Grimes, *J. Phys. Chem. C* 111 (2007) 17527–17534.
- [23] L.A. Silva, S.Y. Ryu, J. Choi, W. Choi, M.R. Hoffmann, *J. Phys. Chem. C* 112 (2008) 12069–12073.
- [24] K. Li, M. Han, R. Chen, S.L. Li, S.L. Xie, C. Mao, X. Bu, X.L. Cao, L.Z. Dong, P. Feng, Y.Q. Lan, *Adv. Mater.* 28 (2016) 8906–8911.
- [25] J. Sun, L. Gao, Q. Zhang, *J. Am. Ceram. Soc.* 86 (2003) 1677–1682.
- [26] D.C. Look, D.C. Reynolds, C.W. Litton, R.L. Jones, D.B. Eason, G. Cantwell, *Appl. Phys. Lett.* 81 (2002) 1830–1832.
- [27] S. Mishra, A. Ingale, U.N. Roy, A. Gupta, *Thin Solid Films* 516 (2007) 91–98.
- [28] O. Zelaya-Angel, F.d.L. Castillo-Alvarado, J. Avendaño-López, A. Escamilla-Esquivel, G. Contreras-Puente, R. Lozada-Morales, G. Torres-Delgado, *Solid State Commun.* 104 (1997) 161–166.
- [29] R. Rossetti, S. Nakahara, L.E. Brus, *J. Chem. Phys.* 79 (1983) 1086–1088.
- [30] W. Wang, Z. Liu, C. Zheng, C. Xu, Y. Liu, G. Wang, *Mater. Lett.* 57 (2003) 2755–2760.
- [31] S.-H. Wei, S.B. Zhang, A. Zunger, *J. Appl. Phys.* 87 (2000) 1304–1311.
- [32] Q. Li, B. Guo, J. Yu, J. Ran, B. Zhang, H. Yan, J.R. Gong, *J. Am. Chem. Soc.* 133 (2011) 10878–10884.
- [33] J.L. Gole, J.D. Stout, C. Burda, Y. Lou, X. Chen, *J. Phys. Chem. B* 108 (2004) 1230–1240.
- [34] H. Kato, K. Asakura, A. Kudo, *J. Am. Chem. Soc.* 125 (2003) 3082–3089.
- [35] Y. Wang, Q. Wang, X. Zhan, F. Wang, M. Safdar, J. He, *Nanoscale* 5 (2013) 8326–8339.
- [36] D. Sarkar, C.K. Ghosh, S. Mukherjee, K.K. Chattopadhyay, *ACS Appl. Mater. Interfaces* 5 (2013) 331–337.
- [37] W. Zhao, W. Ma, C. Chen, J. Zhao, Z. Shuai, *J. Am. Chem. Soc.* 126 (2004) 4782–4783.